Lab on a Chip

PAPER

View Article Online
View Journal

Cite this: DOI: 10.1039/d5lc01063b

Lyocell–modal thread microfluidic platform integrated with a microneedle sensor for lactate detection in saliva

Ling Ding, Huizi Zhang, Yao Li and Jun Kameoka *

The advancement of wearable and point-of-care (POC) biosensing technologies has driven a growing demand for microfluidic substrates that are flexible, hydrophilic, and compatible with electrochemical sensing. In this study, a lyocell-based thread microfluidic platform was developed to overcome limitations of conventional microfluidic systems. The device employs polypropylene (PP) mesh as a structural substrate and is coupled with a modal absorption pad to sustain consistent and continuous liquid transport. Lyocell's inherent capillary-driven wicking, superior hydrophilicity, semicrystalline microstructure, and high wet modulus collectively provide excellent liquid transport efficiency, structural stability under wet conditions, and bubble-free flow. Experimental analysis revealed that unmodified lyocell achieved liquid transport velocities comparable to plasma-treated cotton, confirming its intrinsic capillary efficiency. When integrated with a microneedle-based electrochemical sensor, the device demonstrated rapid analyte delivery and stable signal generation for both ferrocyanide and lactate detection. The thread-integrated lactate sensor exhibited a strong log-linear correlation, with limits of detection (LoD) of 0.433 mM using chronoamperometry (CA) and 0.51 mM using differential pulse voltammetry (DPV). Human saliva testing was also conducted using saliva samples, and the results were compared with blood lactate concentrations. A strong correlation was observed between salivary and blood lactate levels (R = 0.94). Overall, the lyocell–modal hybrid microfluidic platform provides a sustainable, low-cost, and scalable strategy for electrochemical point-of-care testing (POCT), offering a promising route toward next-generation lab-on-fabric systems.

Received 18th November 2025,
Accepted 19th March 2026

DOI: 10.1039/d5lc01063b

rsc.li/loc

Introduction

Microfluidics first emerged in the 1980s for precise microscale chemical synthesis[1] and biological manipulation.[2] Early devices relied on rigid substrates such as silicon and glass to maintain the channel geometry and stable flow control, but these materials were brittle and expensive, and required complex cleanroom microfabrication processes as well as external pumps and tubing.[3–5,7] In the 1990s, polydimethylsiloxane (PDMS) became a widely adopted alternative due to its low cost, optical transparency, biocompatibility, and rapid prototyping capability,[6,8] which significantly accelerated biochemical[9,10] and lab-on-a-chip research.[10,11] However, PDMS lacks mechanical durability, and its adhesion deteriorates under moisture, oils, or sweat, leading to delamination in flexible or wearable formats.[4,12] Since the 2010s, the rise of wearable and point-of-care biosensing technologies—including veterinary testing,[13,14] personal healthcare,[15] and portable diagnostics[16]—has driven the need for hydrophilic, flexible, and low-cost materials that support seamless, skin-interfaced, and power-free microfluidic operation for real-time physiological monitoring.

Paper, composed of a porous network of cellulose fibers, was introduced as a low-cost microfluidic substrate to overcome some limitations associated with traditional PDMS-based systems.[17,18] Paper-based microfluidics can passively wick fluids by intrinsic capillary action, eliminating the need for external pumping systems. Recent studies have further expanded the capabilities of paper-based fibrous microfluidics to more advanced sample-processing tasks, such as humidity-enhanced plasma separation on Chinese Xuan-paper, highlighting the broader diagnostic potential of capillary-driven porous materials.[19] Nevertheless, paper-based microfluidic devices often suffer from limited flow precision and poor reproducibility,[22,23] because their performance is strongly influenced by environmental humidity, temperature, and intrinsic paper porosity.[4,20,24] In addition, paper exhibits poor mechanical robustness, making it fragile and prone to tearing or deformation, and lacks durability under repeated mechanical stress.[25,26] Furthermore, paper's intrinsically insulating and highly hydrophilic nature 2D design restricts

Waseda University, Graduate School of Information, Production and Systems (IPS), 2-7 Hibikino, Wakamatsu Ward, Kitakyushu, Fukuoka 808-0135, Japan.
E-mail: jkameoka@waseda.jp

its compatibility with conductive inks and electrode materials, thereby impeding its integration with electrochemical and electronic sensing components.[20] To achieve multi-step assays or vertical flow paths, paper-based microfluidics often require complex multilayer stacking or origami folding structures, which substantially increase fabrication complexity, alignment challenges and risk of leakage.[21,22] These limitations restrict the potential of paper materials as a practical platform for advanced electrochemical biosensing application, where stable integration and reliable performance of highly sensitive electrodes are severely hindered by the insulating and moisture-absorptive matrix of paper. As a result, alternative fibrous materials are increasingly being explored for electrochemical microfluidic applications.

Thread-based microfluidic systems have emerged as a promising alternative to address the limitations of paper-based platforms and to enhance biosensing applications.[27,28] In thread-based systems, single fibers, or yarns – such as cotton,[33] polyester,[34] or silk[35] – serve as capillary microchannels that enable passive liquid transport, making them suitable for routing sweat or wound exudate to sensing sites.[37,38] Meanwhile, characterized with fibrous networks, thread fibers provide continuous capillary pathways that improve directional control and fluid transport precision, and the filamentous structure of thread also improves tolerance to bending, twisting and tensile deformation while maintaining continuous capillary pathways. In addition, thread-based platforms are more compatible with electrochemical integration because their linear geometry allows direct contact between the fluidic pathway and electrode surface without the need for complex multilayer stacking or origami folding.[4,31] Moreover, the intrinsic softness, flexibility, and breathability of textile fibers also impart superior mechanical durability and conformability, which are also properties essential for on-skin and wearable integration. Accordingly, thread-based microfluidics have been investigated as platforms for wearable biosensing,[28] sweat analysis,[4] and on-body diagnostics,[32] and these studies highlight the potential of thread-based microfluidics for physiological monitoring and wearable biosensing.[20] Besides these applications, thread-based platforms have also been extended to POCT bioanalysis, including rapid blood typing on cotton thread-based analytical devices and, more recently, 3D single-thread microfluidic devices for smart blood typing, demonstrating that thread substrates can support increasingly sophisticated diagnostic functions beyond simple fluid transport.[29,30]

Despite these advances, however, conventional thread materials still present important challenges in electrochemical sensing. Uneven fiber packing density and variable capillary pathways often lead to inconsistent liquid flow rates and unpredictable fluid retention, thereby undermining quantitative assay reproducibility.[36,39] In addition, electrode integration with thread-based microfluidic systems is hampered by poor wet-state stability and weak adhesion at the liquid–electrode interface, which may lead to delamination or signal drift when the substrate is bent, flexed, or saturated by fluid.[40–42] In addition, reliable electrochemical sensing requires stable electrical conduction across fiber-to-fiber contacts, whereas many traditional thread materials show unstable inter-fiber electrical pathways, causing baseline drift, increased noise, bubble formation, and poor repeatability of sensor signals.[39,43,44] These limitations indicate the need for textile materials with more uniform microstructures with electrochemical interfaces.

In this work, we address these limitations using a lyocell-based thread microfluidic platform integrated with a ferrocyanide and lactate microneedle electrochemical sensor to identify lyocell as a highly promising material for fluid transport stability and electrochemical sensing performance in microfluidics devices. Lyocell is a 100% regenerated cellulose fiber with a highly uniform microstructure, providing far more consistent capillary flow than natural fibers such as cotton.[43,45] Lyocell is an excellent thread material for microfluidics with intrinsic hydrophilicity and high wet modulus, enabling more consistent capillary transport than natural fibers.[46–48] To further sustain liquid transport, a modal absorption pad was incorporated at the outlet because modal exhibits high water absorbency, large liquid-holding capacity, and rapid drying behaviour.[49,50] Lactate was selected as a target analyte because it is an important biomarker for metabolic activity, exercise intensity, fatigue, and tissue perfusion, making it highly relevant for point-of-care (POCT) monitoring. In addition to sweat analysis, saliva represents an attractive biofluid for lactate sensing because it can be collected noninvasively, repeatedly, and with minimal discomfort, which is advantageous for POCT testing and continuous health assessment. Since lactate levels in saliva are generally lower than those found in sweat, sensitive and stable microfluidic-electrochemical platforms are required for reliable detection. By combining lyocell microfluidic channels, a modal absorption pad, and a microneedle electrochemical sensor, the proposed platform provides stable analyte delivery and a favourable wet-state environment for continuous electrochemical detection. The lyocell–modal hybrid system demonstrates rapid and uniform fluid transport together with reliable ferrocyanide and lactate sensing, highlighting the promise of lyocell for next-generation lab-on-fabric biosensing.

Materials and fabrication

Materials and reagents

Thread device. The thread-based device is composed of lyocell thread, polypropylene (PP) screen-printing mesh, and a modal absorption pad. Lyocell thread was purchased from Amazon. Polyester screen-printing mesh was purchased from Monotaro. The modal absorption pad was purchased from Comonsava.

Microneedle sensor. The microneedle sensor is fabricated using three acupuncture needles purchased from SEIRIN Point (0.16 × 30 mm in size) that were sequentially coated with multiple chemical layers. Carbon sensor paste (C2070424P2, SunChemical) and Ag/AgCl ink (BAS Inc.) were used for working and reference electrodes, respectively. Carboxyl-functionalized multiwalled carbon nanotubes (MWCNT-COOH; Sigma-Aldrich) were employed as a conductive modifier. EDC (1-ethyl-3-(3-dimethylaminopropyl) carbodiimide HCl) and NHS (*N*-hydroxysuccinimide) (Thermo Scientific) were dissolved in MES buffer (pH 6, Bio-World) to prepare the coupling solution. Lactate oxidase (LOX, 47.5 U mg^{-1} solid) and sodium L-lactate (~98%, both from Sigma-Aldrich) were used as the enzyme and substrate, respectively. The MWCNT-COOH dispersion (0.8 mg mL^{-1}) was prepared in purified water, while EDC (80 mM) and NHS (120 mM) were freshly mixed in MES buffer (pH 6). Lactate solutions (0.001–10 mM) and LOX solution (30 U mL^{-1}) were prepared in 0.1 M phosphate buffer (pH 7).

Fabrication of the lyocell-based thread microfluidic device

Fig. S1 shows a photograph of the lyocell-based thread microfluidic device integrated with a modal absorption pad. The entire assembly was fabricated by stitching a single-strand lyocell thread onto a rectangular polypropylene (PP) mesh (3.5 × 2.5 cm). The first stitch was placed at the inlet area, where a 0.5 × 0.75 cm square area was sewn using a single-yarn, horizontal zigzag stitching pattern, providing bilateral liquid absorption surfaces on both sides of the PP mesh. For the subsequent assembly, a hidden stitching technique was employed to ensure that the lyocell thread was exposed only on the upper surface of the polypropylene (PP) mesh. This configuration confined liquid transport to a single plane and established a well-defined, unidirectional wicking pathway that guided the fluid toward the distal modal absorption pad. Following the inlet area, three parallel lyocell pathways were sewn to serve as liquid transport channels. This configuration was determined to provide an optimal balance between flow velocity and capillary uniformity, as a single pathway yielded insufficient flow rate. At the downstream end, a 0.5 × 1 cm sensing area was stitched using the same technique and connected to the three-transport pathway.

Finally, a modal absorption pad was added to enhance the microfluidic system. The interface area of the lyocell-based thread microfluidic device is approximately 8.75 cm^2, and the device is designed for continuous operation for 2 hours. According to Pietro Salvo *et al.*, the maximum sweat generation rate that can be reached during intense physical activity is 40 g m^{-2} h^{-1}, corresponding to about 70 μL cm^{-2} h^{-1} when scaled to the lyocell thread interface area.[51] To ensure adequate fluid accommodation during operation, a 2 × 2 cm modal absorption pad was incorporated at the outlet; its dimensions were optimized based on the liquid absorption and spreading test of modal fibers (Fig. S1). The modal absorption pad was affixed to the PP mesh at three stitch points along its lower edge, defining the liquid outlet region. This component efficiently collected all fluid transported through the lyocell channels, enhanced flow continuity, and acted as a terminal reservoir for excess liquid, thereby facilitating rapid fluid transfer and improving overall device responsiveness during operation.

Fabrication process of the microneedle-based sensor

Three acupuncture needles were used as substrates for fabricating the microneedle-based electrochemical sensor, and Fig. 1 illustrates the complete fabrication process for ferrocyanide and lactate microneedle sensors. To enhance coating adhesion, the stainless-steel surface of each microneedle was mechanically polished with fine sandpaper to increase surface roughness. The polished needles were ultrasonically cleaned in purified water for 5 minutes and air dried prior to surface modification. Herein, the fabrication process of the ferrocyanide microneedle sensor is described. For the reference electrode, the polished microneedle surface was uniformly coated with Ag/AgCl paste and oven-dried at 120 °C for 10 minutes. After cooling to room temperature for 10 minutes, the needle was ready for use. For the counter electrode, the stainless needle surface was coated with carbon sensor paste and oven-dried and crosslinked at 120 °C for 10 minutes, followed by room-temperature cooling for 10 minutes. The electrode was then designated as the counter electrode. For the working electrode, the microneedle surface was coated with carbon sensor paste and oven-dried at 120 °C for 10 minutes. After cooling, multi-walled carbon nanotubes (MWCNT-COOH, 0.8 mg mL^{-1} in purified water) were electrodeposited by cyclic voltammetry between −0.5 V and +0.5 V for 15 cycles at 0.1 V s^{-1} using an EmStat4S potentiostat. The electrode was then rinsed with PBS and air-dried at room temperature.

The working electrode for the lactate sensor was prepared following the same procedure as the ferrocyanide sensor. After coating with carbon sensor paste containing Prussian blue and MWCNTs, additional surface functionalization was needed. A mixed activation solution containing EDC (80 mM) and NHS (120 mM) in buffer (pH 6.0) was drop-cast (0.25 mL) onto the MWCNT-modified surface for 25 minutes at room temperature. The surface was then rinsed with PBS to restore the neutral pH (~7). Thereafter, 0.1 mL of lactate oxidase solution (30 U mL^{-1} in PBS) was drop-cast onto the microneedle working electrode surface for 1 hour at room temperature. After drying, the enzyme-immobilized microneedle was used as the working electrode for lactate sensing.

After preparation, the reference, counter, and working electrodes for both ferrocyanide and lactate sensors were assembled into a quasi-triangular arrangement using insulating tape, with an inter-electrode spacing of approximately 0.6 mm between electrodes (photograph

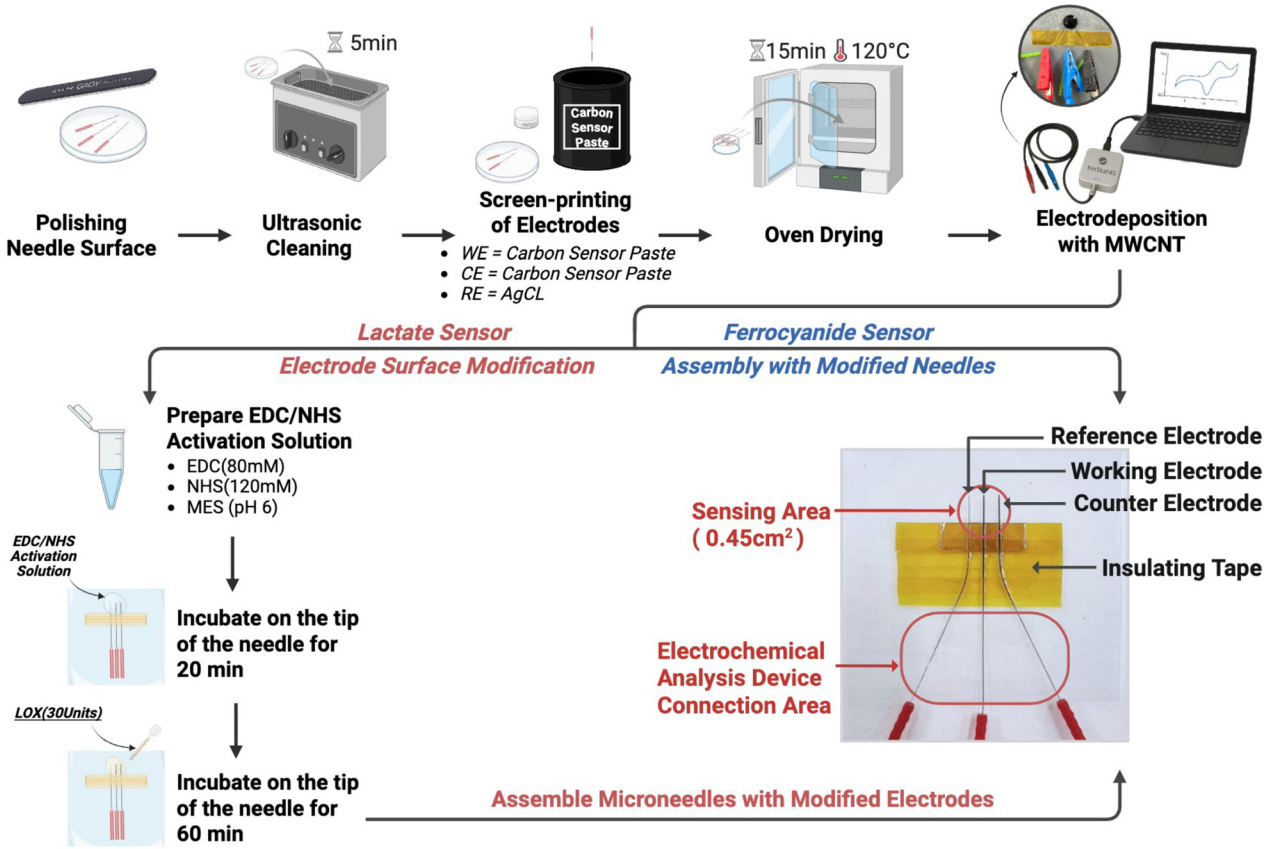

Fig. 1 Fabrication process of the microneedle-based sensor. Stepwise fabrication process for the microneedle-based ferrocyanide sensor and lactate sensor.

Fig. 1). An initialization step was performed for the lactate sensor prior to measurement by applying a constant potential of −0.25 V in chronoamperometric mode in 0.01 mM lactate solution for 5 minutes to stabilize the electrode response.

Integration of the microneedle sensor with the lyocell microfluidic device

Fig. 2 illustrates the integration process of the microneedle sensor with the lyocell–modal-based thread microfluidic device. The microfluidic platform and the microneedle sensor were fabricated separately in the initial step as shown in Fig. 1 and S1. In step 2, the three electrodes of the microneedle array were carefully inserted into the inter-fiber gap located within the sensing area of the lyocell thread. Once properly positioned, a small amount of UV-curable adhesive was gradually drop-cast between the insulating tape and the PP mesh to fix the positions of the three electrodes. In step 3, after an even adhesive layer was formed, it was immediately cured under UV light to solidify the adhesive layer. This procedure firmly secured the microneedle sensor onto the microfluidic device, ensuring stable electrical contact and mechanical integrity during operation.

Electrochemical sensing mechanism of the lactate sensor

Fig. 3 illustrates the surface chemical configuration of the microneedle-based lactate sensor. A stainless-steel microneedle served as the structural backbone and provided an efficient pathway for electron conduction. Upon carbon sensor paste coating with Prussian blue as a mediator, a stable and highly conductive interface was formed. The immobilization of multiwalled carbon nanotubes (MWCNTs) functionalized with carboxyl groups (–COOH) provided abundant reactive sites and enhanced sensitivity for EDC/NHS-mediated activation. During the activation step, the carboxyl groups (–COOH) were first activated by EDC to form an unstable *O*-acylisourea intermediate, which was subsequently stabilized through NHS coupling to yield an NHS ester. This reactive ester enabled covalent attachment of lactate oxidase (LOX) through amine coupling. Upon enzyme immobilization, the terminal amine groups of LOX reacted with the NHS ester to form a stable amide bond between LOX and the MWCNT surface. The immobilized LOX catalyzes the oxidation of lactate into pyruvate, generating hydrogen peroxide (H_2O_2) as a by-product. The produced H_2O_2 was subsequently reduced to water (H_2O) by Prussian blue, leading to efficient electron transfer to the electrode.[52] This

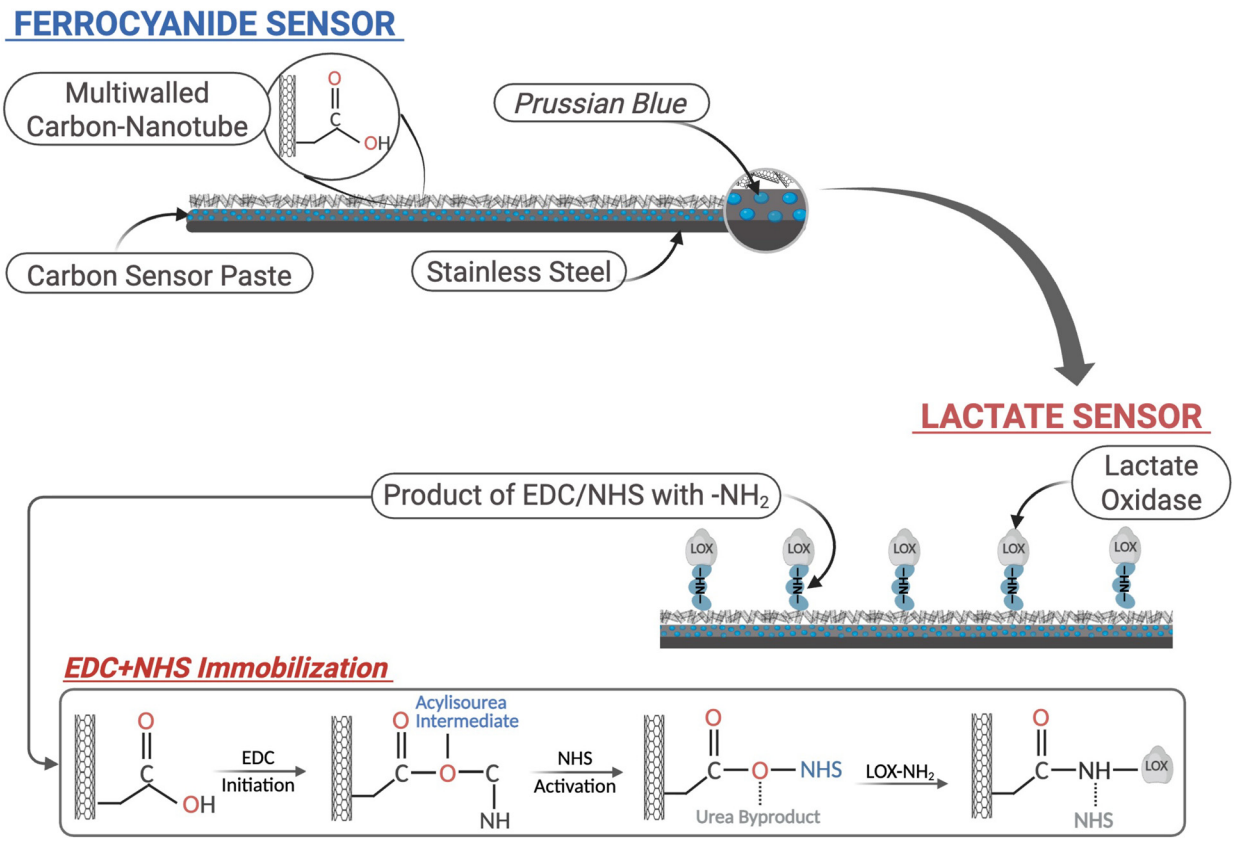

Fig. 2 Surface modification schematic. Schematic illustration of the surface modification of the microneedle-based working electrode for ferrocyanide and lactate detection.

hierarchical configuration ensures robust enzyme immobilization, enhanced catalytic stability, and efficient electron transfer, which contributed to high sensor sensitivity and operational reliability.[52]

Experiments and discussion

Lyocell flow speed analysis

The liquid transport through the single thread was investigated and the experimental setup is shown in Fig. 4a. Four sets of threads were stitched onto the surface of polypropylene (PP) mesh using a single-yarn stitching method. For each group, an identical solution inlet area and an 11 cm-long liquid transport pathway were fabricated. The liquid front displacement and corresponding velocity were recorded at 1, 3, and 5 minutes after the addition of 15 μL dyed solution. Fig. S2a summarizes the results of the liquid transport phenomena among different material threads, with and without plasma treatment.

Kinematic analysis revealed that lyocell exhibited a remarkably higher liquid transport rate and greater penetration distance compared to cotton, both before and after plasma treatment. Fig. 4b and c visualize the change in transport distance and velocity over the first 300 seconds, respectively.

From Fig. 4b, non-plasma-treated lyocell showed nearly the same transport distance as plasma treated cotton, and even exceeded it within the first minute. In contrast, non-plasma-treated cotton showed negligible improvement throughout the entire experiment. Plasma-treated lyocell displayed the highest liquid penetration distance, confirming the superior capillary wicking ability of lyocell fibers without modifications. These results collectively indicated that lyocell inherently possesses excellent liquid transport capability.

From Fig. 4c, all thread types reached their peak flow velocity within the first minute. The velocity ranking from highest to lowest was plasma-treated lyocell, non-plasma-treated lyocell, plasma-treated cotton, and non-plasma-treated cotton. Notably, non-plasma-treated lyocell exhibited a velocity 0.17 mm s^{-1} higher than plasma-treated cotton, corresponding to a 147% increase over non-plasma treated cotton. This clearly demonstrates lyocell's outstanding liquid transport efficiency. At 3 minutes and 5 minutes, plasma-treated cotton slightly surpassed non-plasma treated lyocell by only 0.028 mm s^{-1} and 0.017 mm s^{-1}, respectively – differences that were within experimental variation. These observations further confirm that even non-plasma-treated lyocell achieves liquid transport performance comparable to plasma-treated cotton. Furthermore, plasma-treated lyocell achieved a peak velocity 1.5 times higher than that of plasma-treated cotton which highlighted its superior

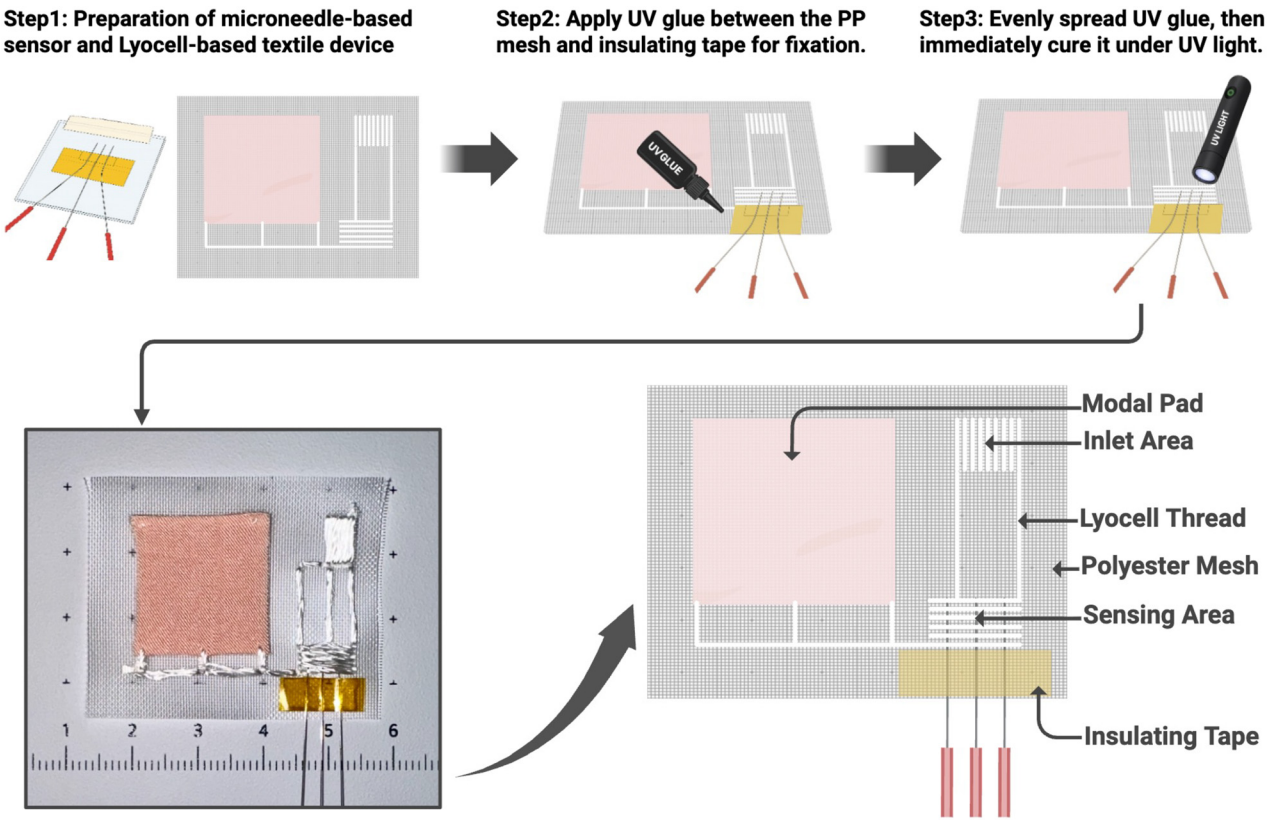

Fig. 3 Schematic diagrams of the microneedle sensor surface for ferrocyanide and lactate sensing. Both sensors employ a stainless-steel substrate coated with carbon sensor paste containing Prussian blue and an electrodeposited MWCNT-COOH layer. For lactate sensing, lactate oxidase (LOX) is covalently immobilized *via* EDC/NHS coupling, where carboxyl groups (–COOH) are activated by EDC and stabilized by NHS to form reactive NHS esters, enabling stable amide bond formation with LOX.

capillary-driven wicking potential. Most natural fibers such as cotton show inherently hydrophobic behavior because their outer layers contain waxes, fats and pectin, therefore they require surface modification to promote wicking and capillary flow. Lyocell fibers were regenerated with their pure cellulosic composition and abundant hydroxyl (–OH) groups, which make them intrinsically hydrophilic and enable rapid wetting without surface modification.[49] Additionally, their nanoscale pores between cellulose chains and the smooth fiber surface further facilitate fast, unobstructed fluid transport through the thread network.

These results confirm that lyocell, even in its native state, provides exceptional fluidic performance for thread-based microfluidic systems surpassing the performance of most conventional thread substrates and rendering additional plasma treatment optional rather than essential.

Liquid transportation analysis of the lyocell-based thread microfluidic device

A time-lapse experiment was conducted to evaluate the liquid transport in the lyocell-based thread microfluidic device (Fig. 5a). Initially, 20 μL of deionized (DI) water was first dispensed into the inlet area, and the corresponding wetted area on the modal pad was recorded. After 2 minutes, an additional 15 μL of DI water was dispensed into the inlet area every 3 minutes to simulate continuous fluid delivery. Fig. 5b presents the cumulative liquid volume transported from the inlet area to the distal modal absorption pad over a 20 minute period, where the transported volume was estimated based on the wetted area to liquid volume conversion equation obtained from Fig. S1c and d. Fig. 5c illustrates the time lapse of flow rate, calculated by dividing the transported liquid volume by elapsed time. In Fig. 5c, the flow rate increased progressively during the first 12 minutes and reached equilibrium at approximately 12–15 minutes. This behavior can be attributed to the gradual filling of the three stitched junctions connecting the lyocell channels and modal absorption pad as shown in Fig. 5a–d. After this point, the flow rate stabilized, indicating the establishment of steady-state liquid transport through the thread microfluidic network. These findings further confirm that the lyocell–modal structure enhanced the wicking capability which enabled a continuous liquid flow through the upstream lyocell channels without the need for external pumping. In addition, it also effectively prolongs the time required for the lyocell-based thread device to reach saturation. In the absence of the modal component, the liquid front would likely reach equilibrium much earlier, resulting in a rapid drop in transport velocity. This also demonstrates that the

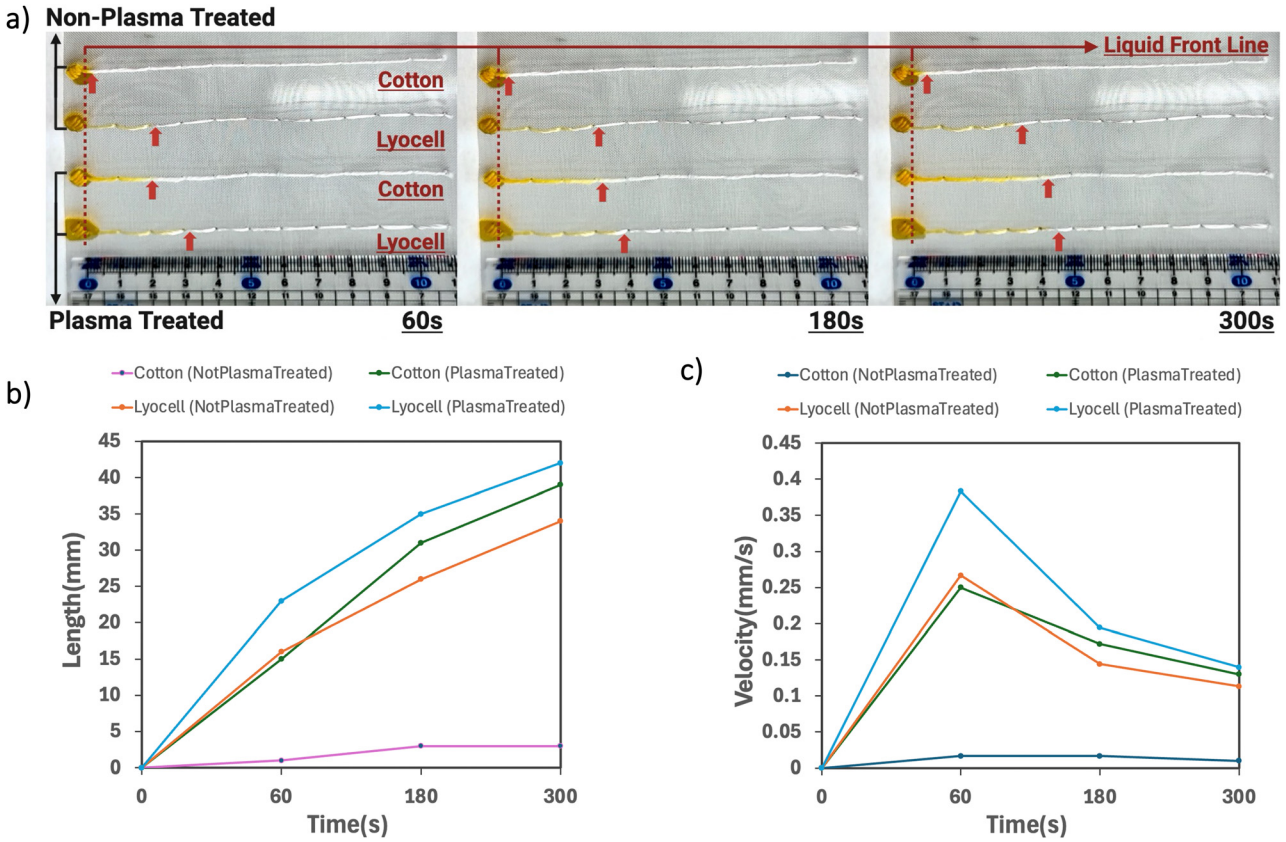

Fig. 4 Thread liquid transport analysis. (a) Photograph of the experimental setup, captured 600 minutes after liquid dispensing. (b) Line plot shows the displacement of liquid transport over time for plasma-treated and non-plasma-treated lyocell and cotton threads. (c) Line plot shows the variation in liquid transport velocity within the first 5 minutes for plasma-treated and non-plasma-treated lyocell and cotton threads.

lyocell–modal microfluidic system exhibits a controlled and reproducible water retention rate, enabling the thread to maintain consistent hydration. This behavior is particularly advantageous for thread-based microfluidics, as it allows the fluid volume and wicking performance to be precisely controlled and predicted during electrochemical testing.

Therefore, the lyocell–modal hybrid configuration not only enhances liquid-handling capacity but also demonstrates strong potential for continuous monitoring applications, characterized by its rapid initial uptake and stable, sustained capillary-driven flow without the need for external pumping.

Electrochemical performance of thread devices fabricated from lyocell, cotton and wool

A comparative experiment was conducted to evaluate the electrochemical sensing performance of the lyocell-based thread device for ferrocyanide detection, in comparison with devices fabricated from cotton and wool threads (Fig. 5d), and all the threads were prepared without plasma treatment. Three thread microfluidic devices were respectively prepared using lyocell, cotton and wool threads, with each platform integrated with an identical microneedle-based ferrocyanide sensor. During chronoamperometric (CA) measurements, 20 μL of 40 mM ferrocyanide solution was sequentially dispensed into the inlet area of each device every 30 seconds. The sequential additions correspond directly to the current peaks observed in Fig. 5e.

As shown in Fig. 5e, the sensor integrated with the lyocell-based thread device exhibited the fastest electrochemical response, initiating immediately when the liquid first reached the sensing area. The lyocell-based device responded at approximately 25 s, which was about 100 s earlier than the wool-based device and 125 s earlier than the cotton-based device. Once the sensing area became fully wetted, a sharp increase in current was observed at around 120 s, followed by a gradual decay and stabilization at approximately 8 μA. An increase in current was observed after each liquid addition, which quickly stabilized to the steady-state current, indicating a stable and consistent current response for ferrocyanide detection. As shown in Fig. S1b, lyocell presents a uniform, circular, fiber cross-section and highly ordered cellulose microfibrils which can minimize air entrapment within fiber bundles and enable rapid wetting of the electrode interface. Therefore, this proves that lyocell provides a stabilized inner-fiber environment that facilitates an efficient electron transfer during electrochemical sensing.

In contrast, the wool-based thread device reached its maximum current at around 180 s and stabilized near 8 μA after approximately 400 s, which was much slower than the

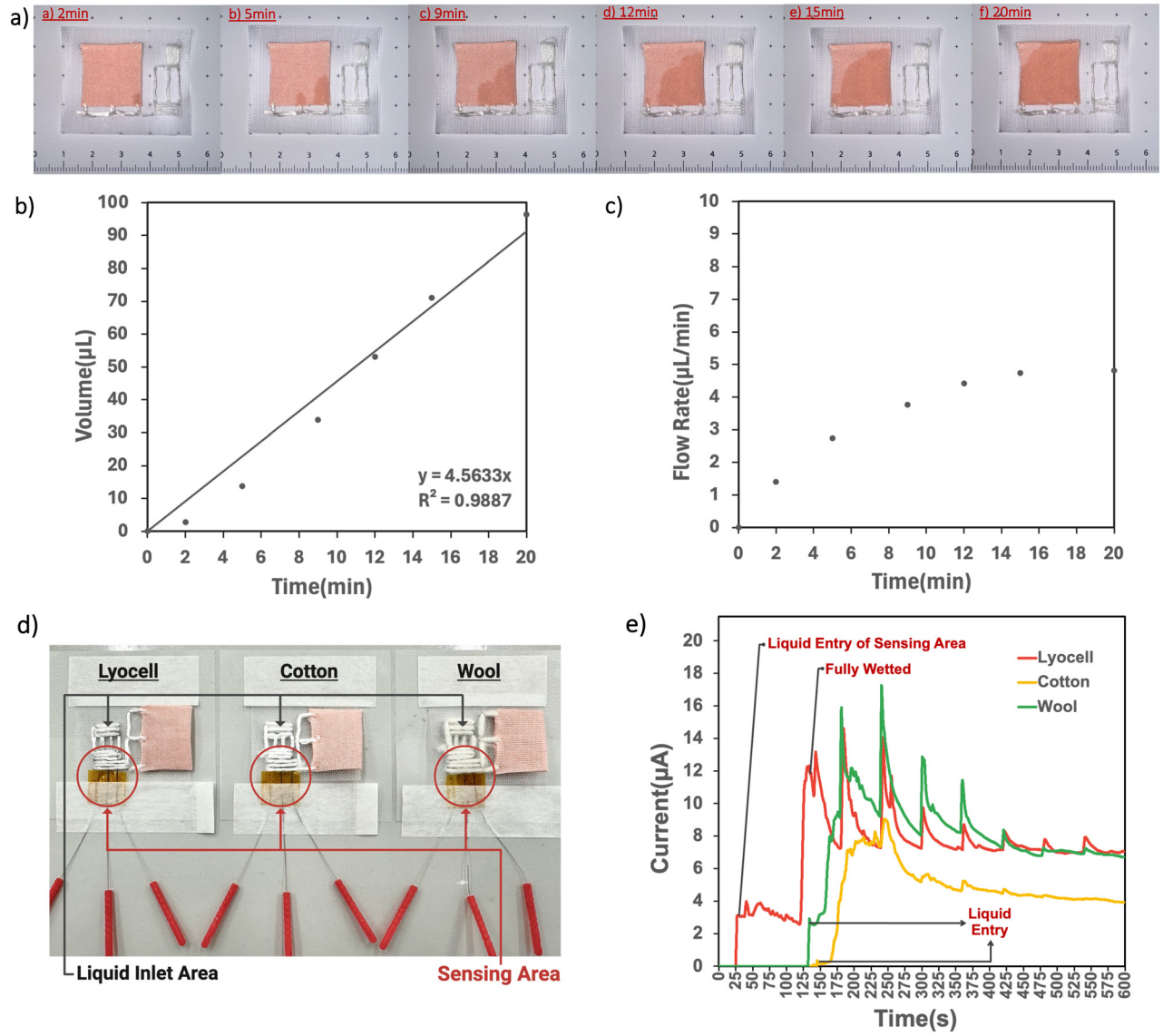

Fig. 5 Lyocell-based thread microfluidic system analysis. (a) Time-lapse photographs showing the liquid flow behaviour within the lyocell-based thread device from 2 to 20 minutes. (b) Dot plot with fitted line illustrating the relationship between transported liquid volume (from the inlet area to the modal absorption pad) and time over a 20 minute period. (c) Dot plot showing the variation of liquid transport velocity over time. (d) Experimental set-up for lyocell-, cotton- and wool-based thread devices used to evaluate and compare electrochemical performance. (e) Chronoamperometric (CA) responses of ferrocyanide sensors integrated with lyocell-, cotton- and wool-based thread devices over a 10 min period. Throughout the measurement, 20 μL of 40 mM ferrocyanide solution was sequentially dispensed into the input region of the thread device every 30 s.

lyocell-based device. The electrochemical signal from the wool platform is higher than that of lyocell after 175 s which can be attributed to the saturation of the modal pad reaching a steady flow rate, as shown in Fig. 5c. This higher signal response was likely due to the larger cross section area of wool fibers compared with lyocell, which facilitates greater electrolyte transport, as observed under an electrical optical microscope (Fig. S1b). However, despite this slightly higher delayed signal, lyocell remains more advantageous for real-time monitoring because its faster wicking enables earlier analyte delivery and more rapid signal stabilization.

The cotton-based device exhibited the slowest liquid transport and poorest electrochemical response, which reached its peak at 250 s and stabilized at a significantly lower steady-state current of about 4 μA, nearly half of that observed for lyocell and wool. Lyocell outperformed cotton due to its smoother and more uniform fiber morphology and smaller cross-sectional area, which promote continuous capillary channels and efficient electrolyte transport. In contrast, the tightly packed cross-sectional structure of cotton fibers restricts electrolyte transport and limits capillary wicking.

These results clearly demonstrate the superior liquid transport efficiency and stable electrochemical performance of the lyocell-based thread device. Its rapid response and faster stabilization prove that lyocell fibers facilitate more efficient solution delivery, thereby enhancing the reaction kinetics and enabling faster establishment of a stable current response. Although the peak current gradually decreased with successive liquid additions, this experiment was intended to demonstrate repeated liquid delivery and electrochemical readout rather than uninterrupted long-term continuous monitoring. For the intended saliva point-of-care application, such short-duration repeated measurements remain practical, as the device is designed for rapid discrete analysis. Overall, the prompt electrochemical response and reliable signal stability highlight the strong potential of lyocell-based thread microfluidic systems for real-time electrochemical monitoring applications.

Comparison of the bare microneedle sensor and thread device integrated microneedle sensor

To evaluate the difference in electrochemical responses between the bare microneedle sensor and the sensor integrated with the lyocell-based thread device, chronoamperometric (CA) measurements were performed on both configurations. As shown in Fig. S2a and b, the CA curves represent the current responses for the bare microneedle sensor and thread device integrated sensor in detecting ferrocyanide at concentrations from 10 to 40 mM. The thread-integrated sensor exhibited an approximate 40% reduction in current amplitude across four concentrations compared to the bare microneedle sensor. Despite this decrease, both sensors demonstrated consistent, concentration-dependent current responses, indicating reliable ferrocyanide detection performance.

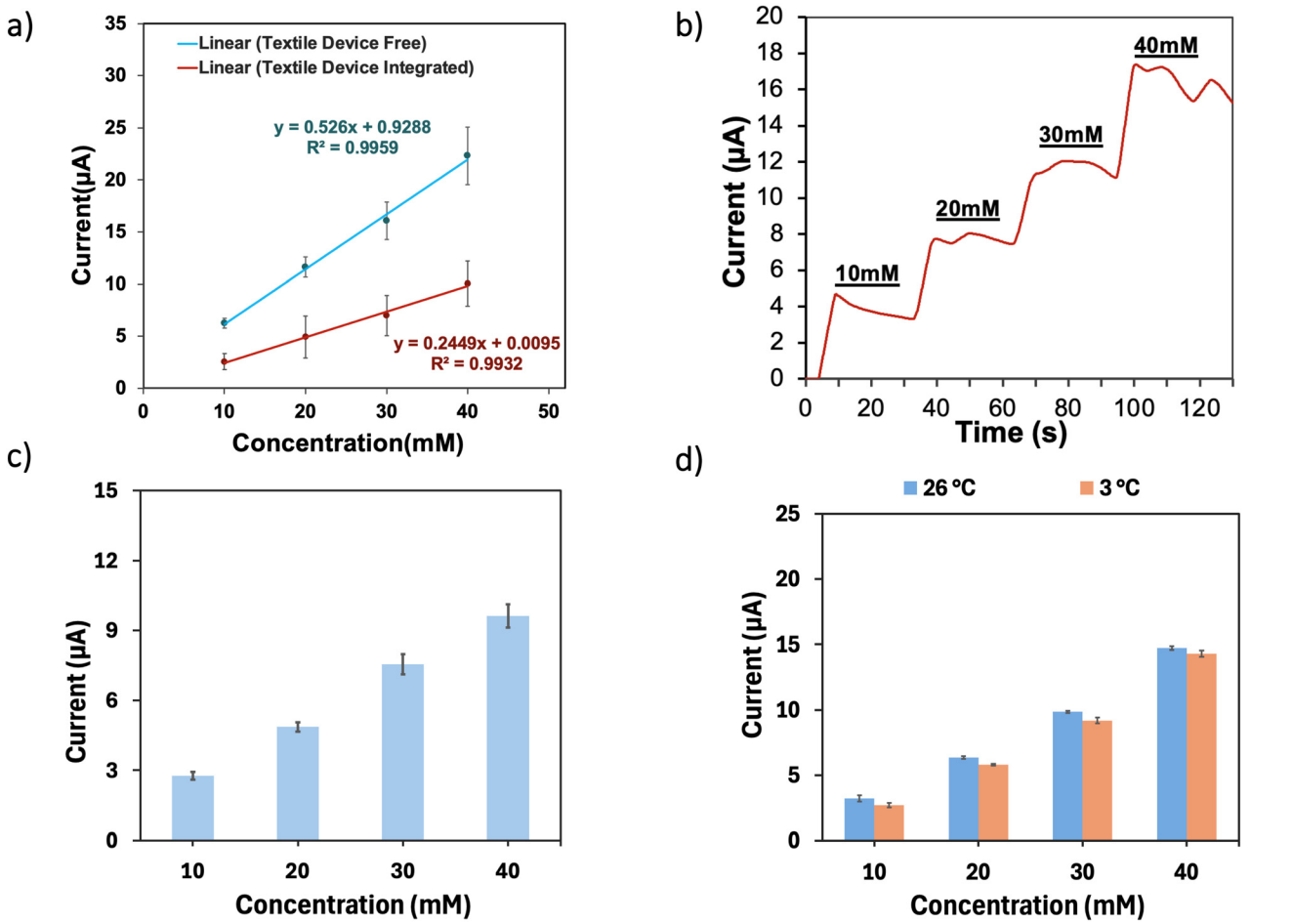

Fig. 6 Electrochemical performance analysis of the microneedle-based ferrocyanide sensor with and without integration of the lyocell-based thread device. (a) Calibration plots comparing the bare and thread-integrated sensors. The upper blue line displays the calibration curve of the bare microneedle sensor, while the lower red line displays the calibration curve of the thread-integrated microneedle sensor (n = 10, mean ± SD). (b) Stepwise chronoamperometric response of the thread-integrated sensor during sequential addition of 20 μL ferrocyanide solutions at concentrations of 10, 20, 30, and 40 mM at 30 s intervals. (c) Reusability evaluation of the lyocell–modal microfluidic device using ferrocyanide. Bar plot showing the current response of the thread-integrated microneedle sensor to 10, 20, 30, and 40 mM ferrocyanide during three washing–testing cycles. Error bars represent the mean ± standard deviation (SD). (d) Electrochemical stability at different temperatures. Bar chart of the thread-integrated microneedle ferrocyanide sensor measured at 26 °C and 3 °C, showing current responses in correlation with ferrocyanide concentration with error bars indicating the mean ± SD.

Fig. 6a compares the calibration curves of the bare microneedle and thread-integrated microneedle sensors. The upper blue line corresponds to the calibration of the bare microneedle sensor, while the lower red line represents the thread-integrated configuration. The bare microneedle sensor exhibited a slope of 0.526 (R^2 = 0.9959), whereas the thread-integrated sensor displayed a slope of 0.224 (R^2 = 0.9826). The slope reflects the sensitivity of the sensor toward ferrocyanide concentration, indicating that while the thread integration slightly reduced signal intensity due to additional diffusion resistance by the thread matrix, both sensors maintained strong linearity and quantitative accuracy ($R^2 > 0.98$). This confirms that the thread-based integration does not compromise the analytical reliability of the microneedle sensor. The error bars represent the standard deviation (n = 10) for both bare and thread-integrated calibration curves. The relatively small SD values across all data points indicate the high repeatability and stable electrochemical performance of the sensor. Moreover, the consistent SD values between the bare and thread-integrated results confirm that the textile integration process did not lead to significant variability in signal output, demonstrating reliable sensor operation both under the textile-free and textile-integrated conditions.

Overall, these results demonstrate that the integration of the microneedle sensor with the lyocell-based thread device preserves strong linearity and analytical sensitivity while improving operational stability, thereby enhancing its potential for reliable, real-time electrochemical sensing in thread-based microfluidic systems.

To further confirm that the thread-integrated sensor can assist the electrochemical sensor in capturing concentration-dependent responses under continuous measurements, an additional chronoamperometric (CA) experiment was performed. Throughout the CA test, 20 μL of ferrocyanide solution at concentrations of 10, 20, 30, and 40 mM was sequentially dispensed into the inlet area of the thread device at 30 s intervals, and the corresponding CA response is shown in Fig. S2b. The sensor exhibited well-defined, stepwise increases in current after each addition, with distinct signal transitions corresponding to each analyte concentration. The presence of stable plateaus and minimal baseline drift between steps indicates rapid signal stabilization and excellent electrochemical responses.

These results demonstrate that the thread-integrated device maintains high responsiveness and stability under continuous operation and confirm its capability to sustain consistent signal transduction during sequential measurements. The stable and stepwise responses suggest that the thread structure helps regulate liquid flow toward the sensing interface, ensuring uniform analyte delivery and minimizing signal fluctuations throughout continuous operations. Overall, these findings indicate the potential of the thread-based platform for continuous electrochemical detection in microneedle-based sensing applications.

Reusability and stability evaluation of the lyocell–modal platform

To evaluate the reusability of the lyocell–modal microfluidic device, the thread-integrated microneedle sensor was tested repeatedly using ferrocyanide solutions at concentrations of 10, 20, 30, and 40 mM for three rounds (washing-and-testing cycles). After each round of testing, the lyocell–modal microfluidic device was washed with PBS five times and dried with a dryer in no-heat mode. The corresponding current responses were recorded after repeated use of the same device platform. The averaged current values were summarized in the bar chart, and the error bars represent the standard deviation of repeated measurements as shown in Fig. 6c. The current response increased progressively with increasing ferrocyanide concentration, which indicated that the lyocell–modal device retained a clear concentration-dependent electrochemical response even after repeated use. The error bars at each concentration indicate acceptable repeatability and stable signal output during washing and testing cycle processes. These results indicate that the lyocell–modal microfluidic device can maintain its fluid transport function and a stabilized electrochemical sensing environment after repeated measurements, which supports its potential for repeated-use applications.

To further determine the influence of temperature on sensor performance, the lyocell–modal integrated microneedle sensor was tested for ferrocyanide detection at 26 °C and 3 °C. Chronoamperometric measurements were used to detect ferrocyanide concentrations at 10, 20, 30, and 40 mM, and the corresponding calibration plots were obtained under both temperature conditions. As shown in Fig. 6d, the sensor exhibited clear concentration-dependent responses at both temperatures. The calibration slope at 26 °C was slightly higher than that at 3 °C, which indicates that the sensor produced a slightly stronger electrochemical response at room temperature. This difference can be attributed to reduced mass transport and slower electrochemical kinetics at lower temperature. However, the overall linear relationship was maintained under both conditions, which demonstrates that the lyocell–modal integrated platform preserved stable sensing performance across the tested temperature range. These results suggest that the device retains acceptable electrochemical functionality at different environmental temperatures, which supports its potential use in practical POCT applications.

Lactate sensor integrated with the lyocell-based thread device

Fig. 7 presents the chronoamperometric (CA) responses of the microneedle-based lactate sensor integrated with the thread-based microfluidic device within the concentration range of 0.01–10 mM. As shown in Fig. S3b, distinct current responses were obtained for each lactate concentration, displaying a clear concentration-dependent increase in current intensity. Fig. 7a illustrates the corresponding calibration curve of steady-state current *versus* the logarithm

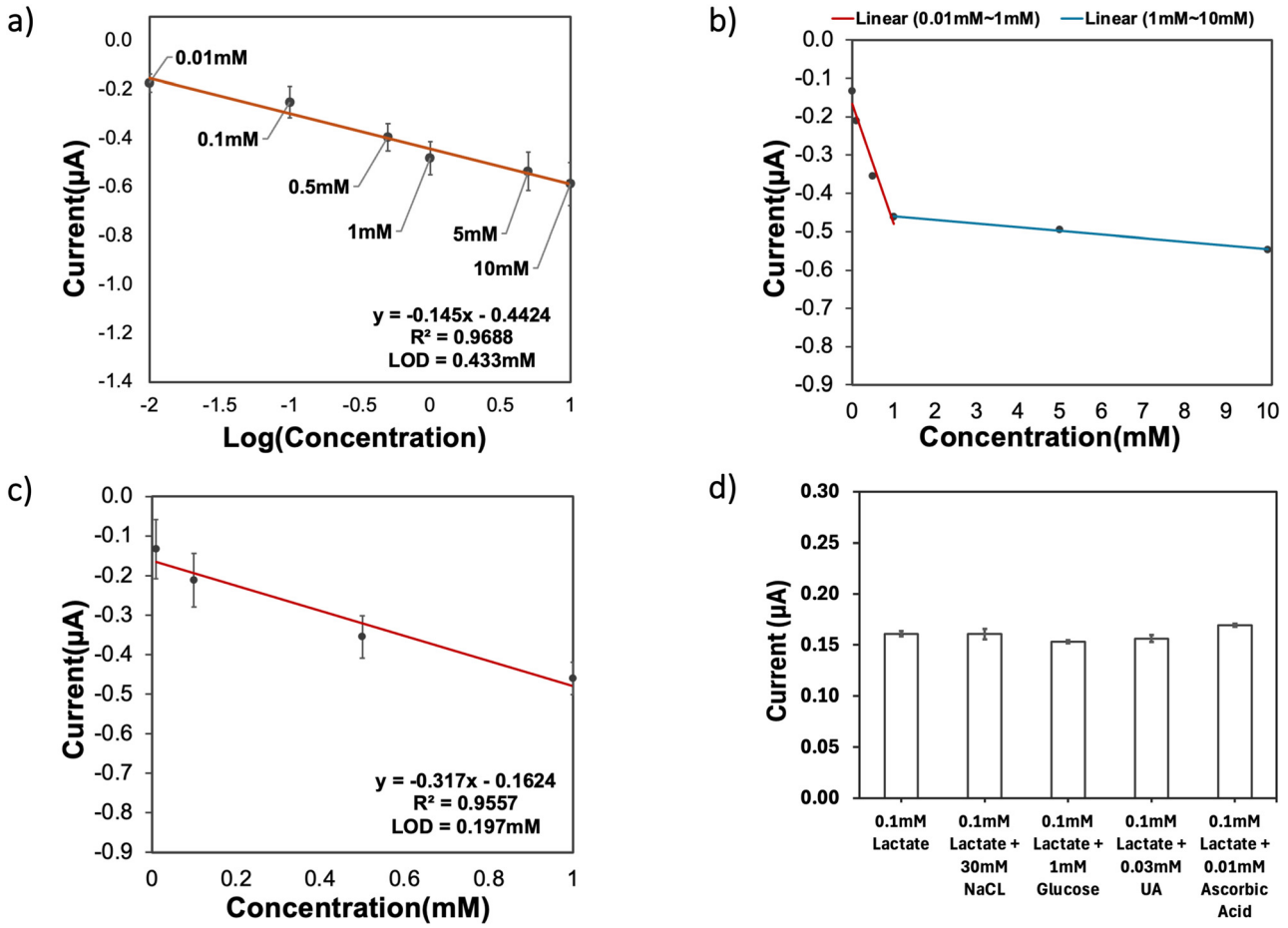

Fig. 7 Lactate sensor integrated with the lyocell–modal thread device. (a) Calibration curve plot (n = 5, mean ± SD) of response current *versus* logarithm of lactate concentration (0.01–10 mM). (b) Relationship between unlogged lactate concentration (0.01–10 mM) and current response, revealing two distinct linear regions. (c) Refined calibration plot (n = 5, mean ± SD) of the lactate concentration (0.01–1 mM) region with a linear correlation (R^2 = 0.9557) with a lower LOD of 0.197 mM. (d) Selectivity analysis of the lactate sensor. Current responses of the lyocell–modal microfluidic device integrated lactate sensor toward 0.1 mM lactate in the absence and presence of common potential interferents, including 30 mM NaCl, 1 mM glucose, 0.03 mM uric acid, and 0.01 mM ascorbic acid. Error bars represent the mean ± SD.

of lactate concentration. A strong log-linear relationship (R^2 = 0.9688) was obtained across the range of 0.01–10 mM, confirming the excellent log linearity and reliable quantitative response of the sensor. This indicates that the measured current is directly proportional to the logarithmic increase in lactate concentration and ensures accurate detection across physiologically relevant levels. The error bar represents the standard deviation (SD, n = 5) of the current response obtained at each logarithmic lactate concentration. The relatively small SD values across the entire range (0.01–10 mM) indicate excellent reproducibility and minimal measurement fluctuation, which demonstrates that the sensor maintained stable electrochemical responses even at low analyte concentrations.

The limit of detection (LoD) was calculated to be 0.433 mM according to the IUPAC criterion (LoD = 3.3 x SD/slope), where SD represents the standard deviation of a blank signal, and the slope corresponds to the linear regression of the calibration curve. This LoD demonstrates the sensor's capability for detecting lactate concentration which falls well within the physiologically relevant range of lactate concentrations typically found in human sweat (1–20 mM).[53] Moreover, the area-normalized sensitivity, based on a 0.0251 cm^2 surface reaction area, was determined to be 5.77 ($\mu A\ mM^{-1}\ cm^{-2}$), which indicated a strong electrochemical response per unit area and concentration. These results confirm the suitability of the thread-integrated device for non-invasive biosensing application.

For comparison, the lactate response of the bare microneedle sensor without the lyocell microfluidic platform is shown in Fig. S3. The bare sensor also exhibited a strong log-linear response over 0.01–10 mM, with R^2 = 0.9762 and a calculated LoD of 0.481 mM. These values are analytically similar to those obtained with the lyocell-integrated device (R^2 = 0.9688, LoD = 0.433 mM), indicating that microfluidic integration does not alter the intrinsic sensing capability of the microneedle electrode. The main advantage of the lyocell platform is that it provides controlled capillary-driven liquid transport and a stable wet-state sensing interface while preserving the analytical performance of the sensor.

As shown in Fig. 7b, the CA results revealed two distinct linear regions between the unlogged lactate concentration (0.01–1 mM) and the current response, corresponding to low (0.01–1 mM) and high (1–10 mM) concentration ranges. In the low concentration region, the sensor exhibited a steeper slope which indicated higher sensitivity. Meanwhile, the response slope decreased beyond 1 mM, which suggested partial saturation of the electroactive surface. To further analyze this effect, Fig. 7c presents the calibration curve focusing on the 0.01–1 mM range, where a linear relationship (R^2 = 0.9557) with small SD (n = 5) values of the current response was obtained. The SD observed in this figure for each concentration point again confirmed high signal stability and repeatability for the lactate sensor integrated with thread microfluidics. The uniformity of SD values further verifies that the integration process and measurement setup introduced consistent performance. The LoD for this range was calculated to be 0.197 mM, also based on IUPAC definition. This lower LoD demonstrates the sensor's capability to resolve small variations in lactate concentration particularly within the physiologically relevant range observed in human saliva (0.11–0.56 mM).[54] The sensitivity was −12.63 (μA mM^{-1} cm^{-2}), calculated from the slope of the calibration curve and normalized to the electrode reaction area (0.0256 cm^2). The favorable analytical performance of the thread-integrated sensor is supported by the lyocell-based thread microfluidic network, which enables controlled analyte delivery and a stable electrochemical sensing surface without compromising the intrinsic sensing capability of the microneedle electrode.

To evaluate the selectivity of the lactate sensor integrated with the lyocell–modal microfluidic device, chronoamperometric (CA) measurements were performed using 0.1 mM lactate in the absence and presence of common interferents. The interferents were selected to represent components that may co-exist in practical biofluids such as human saliva. The selected interferents include 30 mM NaCl, 1 mM glucose, 0.03 mM uric acid (UA), and 0.01 mM ascorbic acid (AA). For each condition, the current response of the thread integrated microneedle lactate sensor was recorded, and the averaged values were calculated in the bar chart. The error bars represent the standard deviation of repeated measurements. As shown in Fig. 7d, the sensor exhibited a stable current response toward 0.1 mM lactate, and in the presence of NaCl, glucose, uric acid, or ascorbic acid. The response remained close to that toward lactate alone under all tested conditions, indicating that the sensor maintained good selectivity toward lactate even in the presence of common coexisting species. These results indicate that the combined effects of the microneedle lactate sensor and the lyocell–modal microfluidic platform provide a stable sensing environment with limited interference from representative saliva- or sweat-related components. Therefore, the integrated device shows promising anti-interference performance for practical biofluid analysis, particularly for saliva POCT applications.

Overall, these results demonstrate that the thread-integrated microneedle-based lactate sensor exhibits excellent linearity, low detection limits, and high sensitivity, underscoring its potential for reliable, continuous, and real-time monitoring of lactate in electrochemical sensing systems.

Lactate sensor stability evaluation

To assess the practical performance of the microneedle-based lactate sensor and provide baseline information for subsequent human saliva measurements, preliminary studies were carried out on its storage stability and ionic conductivity dependent response. First, to evaluate the stability of the bare microneedle-based lactate sensor, the sensor was stored at 26 °C with humidity of 45% and tested by differential pulse voltammetry (DPV) in 0.1 mM lactate on days 1, 3, 6, 9, 12, and 15. The corresponding peak currents are shown in Fig. S3e, and the averaged current values were normalized to the day 1 response and plotted as percentages, with error bars representing the standard deviation of repeated measurements. As shown in Fig. S3d, the sensor maintained a relatively stable response from day 1 to day 6, which indicates good short-term stability at room temperature. After day 9, the peak current gradually decreased with a more pronounced decline by day 15, suggesting progressive loss of sensor activity during storage.

The effect of ionic strength was further investigated because ionic conductivity can strongly influence electrochemical performance. Lactate solutions ranging from 0.01 to 10 mM were prepared separately in 0.5, 0.7, 0.9, and 1 mM PBS, and the sensor response was measured under each condition. As shown in Fig. S5b, concentration-dependent DPV responses were observed in all PBS solutions, whereas both the signal intensity and calibration slope varied with PBS concentration. The highest sensitivity was obtained in 1 mM PBS, indicating that the ionic environment plays an important role in lactate detection and that a higher PBS concentration provides more favorable sensing conditions.

To gain a better understanding of the electrolyte environment, the ionic conductivity of PBS at different concentrations was also measured, as shown in Fig. S5a. A linear relationship was observed between the PBS concentration and ionic conductivity. Based on this relationship, an ionic conductivity of approximately 16 mS cm^{-1} was identified as a favorable condition for lactate detection in human saliva. Accordingly, a calibration plot for subsequent saliva analysis was established using DPV as shown in Fig. 8e. The DPV results showed a strong linear relationship over the concentration range of 0.01 mM to 10 mM, with R^2 = 0.9836 and a limit of detection of 0.51 mM. As shown in Fig. S4b, the well-defined peak responses and small signal variation indicate that DPV provided stable and reliable quantification under the optimized ionic conditions. Meanwhile, DPV was selected for saliva analysis instead of CA because it offers clearer peak definition and improved

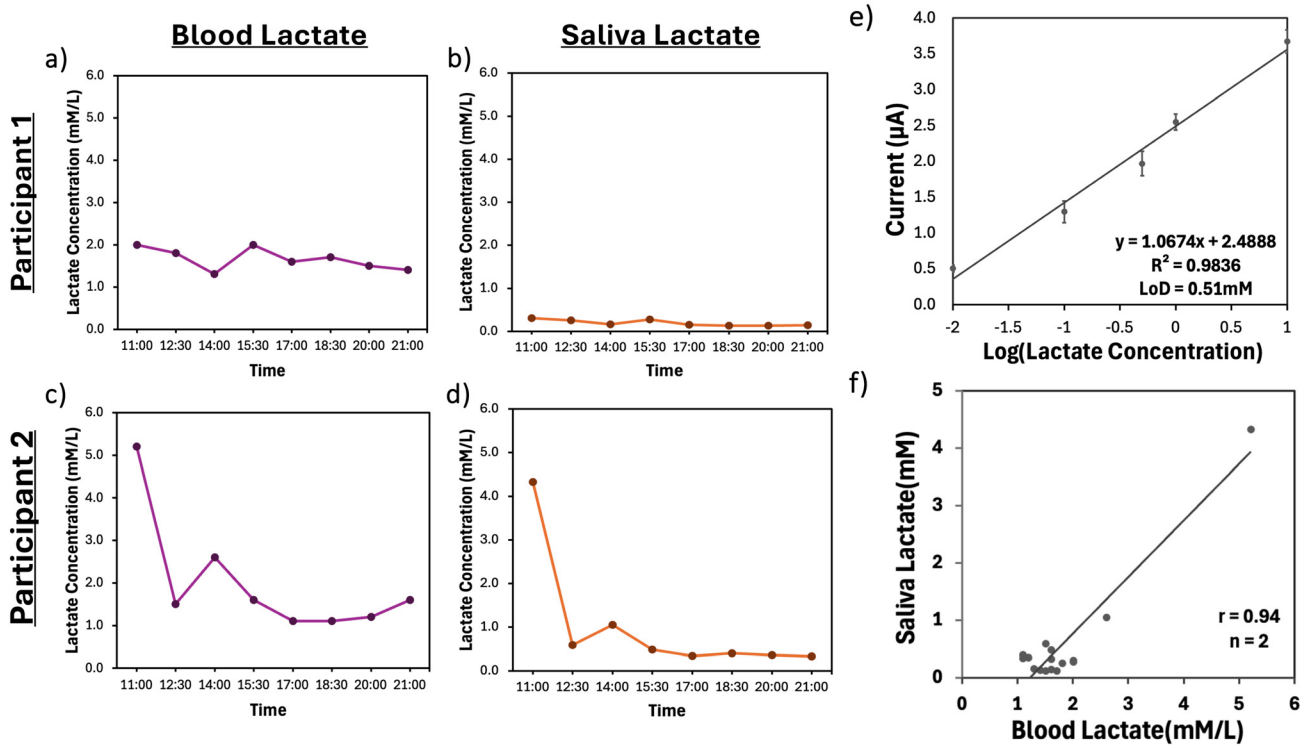

Fig. 8 Human saliva lactate detection and comparison with blood lactate. (a) Time-dependent blood lactate concentration profile of participant 1. (b) Corresponding time-dependent saliva lactate concentration profile of participant 1. (c) Time-dependent blood lactate concentration profile of participant 2. (d) Corresponding time-dependent saliva lactate concentration profile of participant 2. (e) Calibration plot of lactate detection using the microneedle-based lactate sensor integrated with the lyocell–modal device in 1 mM PBS, showing a linear relationship over the concentration range of 0.01–1 mM with R^2 = 0.9836 and LoD = 0.51 mM. (f) Correlation plot between blood lactate and saliva lactate, showing a linear relationship with R = 0.94, n = 2.

signal discrimination at the low lactate concentrations relevant to saliva samples. These results provide important insight into sensor optimization and support the subsequent application of the platform to lactate detection in human saliva.

Lactate detection in human saliva

To address the applicability of the proposed platform for practical biofluid analysis, human saliva samples were collected from two participants at 8 time points throughout the day. Salivary pH, ionic strength, and lactate concentration were monitored, and the saliva lactate results were compared with corresponding blood lactate measurements. Blood lactate concentration was measured using a commercial handheld Eaglenos blood lactate meter (Eaglenos Science, Inc.) and used as the reference for comparison with saliva lactate results. To establish a suitable electrochemical sensing environment for saliva analysis, the pH and ionic strength of each collected saliva sample were first evaluated, as shown in Fig. S5e–l. The salivary pH remained within a relatively narrow range for both participants over the measurement period. In contrast, ionic strength showed a greater variation, which is important because electrolyte conditions can influence the electrochemical sensor response. Based on the ionic-conductivity analysis, PBS-adjustment was introduced to provide a more favorable and controlled sensing environment for saliva measurements. For this adjustment, 4.35 mg PBS powder was always added to 0.5 mL of each saliva sample in vials to increase the ionic strength (16–18 mS cm^{-1}) and adjust the pH (7.2–7.4). As a final step, the saliva samples were dispensed into the inlets in the devices shown in Fig. 3. This treatment reduced the influence of sample-to-sample electrolyte variation and supported more reliable lactate detection.

The time-dependent blood and saliva lactate results are shown in Fig. 8a–d. As shown in Fig. S5c and d, DPV measurements were conducted to evaluate saliva lactate current, and the saliva lactate concentrations were determined from the DPV calibration curve shown in Fig. 8e. In both participants, saliva lactate concentrations were consistently lower than the corresponding blood lactate concentrations, but still exhibited time-dependent variations that broadly followed the changes observed in blood lactate. This agreement indicates that the proposed sensing platform can capture physiologically meaningful lactate trends in saliva despite the lower analyte concentration of saliva. As shown in Fig. 8f, the relationship between saliva lactate and blood lactate showed a strong positive correlation (R = 0.94, n = 2). These results support

the potential of the device as a non-invasive tool for saliva-based lactate assessment and demonstrate that, under controlled ionic conditions, the platform can provide reliable electrochemical readout in a complex biological sample. Although the sample number remains limited, the present results provide a preliminary proof of concept for practical saliva lactate analysis.

Production cost and scalability

The lyocell–modal platform also offers an advantage in terms of production cost. Based on the material usage in this study, the estimated cost of fabricating one device is approximately USD 0.85. This low cost is enabled by using inexpensive fibrous materials and a simple stitching-based assembly process, without the need for complex fabrication. In addition, the ability of lyocell to provide efficient capillary transport without mandatory surface treatment further supports simplified manufacturing. A comparison with commercial and representative lactate sensing platforms is provided in Table S1, which further indicates that the proposed platform has strong potential for low-cost and scalable production in disposable and POCT sensing applications.[55–60]

From a practical perspective, the platform is also compatible with single-use operation. Because the device is composed mainly of low-cost fibrous materials and PP mesh, disposal after a single measurement can be advantageous for bio-fluid analysis to reduce the risk of cross-contamination. The constituent materials of the lyocell–modal device are recyclable in principle as individual components, therefore recycling of the fully assembled device may be possible without addressing the multi-material structure and possible biofluid contamination. Overall, the lyocell–modal platform offers flexibility for either short-term reuse or single-use disposal, depending on the application scenario.

Conclusions

We developed a lyocell-based thread microfluidic platform that overcomes major limitations of conventional microfluidic systems for continuous electrochemical biosensing, offering consistent and continuous capillary-driven flow with controlled liquid retention, robust electrode integration with superior wet-state mechanical stability, and a stabilized inner-fiber microenvironment that enables reliable electrochemical detection. Kinematic tests further demonstrated that unmodified lyocell achieved liquid transport velocities comparable to plasma-treated cotton and can exceed alternatives under identical conditions, confirming its inherent capillary efficiency without the need for surface modification. Fluidic characterization further showed that the combination of lyocell threads and a modal absorption pad – leveraging lyocell's intrinsic hydrophilicity, semi-crystalline structure, and high wet modulus – enabled rapid, stable, and bubble-free capillary transport, while the modal pad maintained a favorable pressure gradient to prevent oversaturation and backflow. Comparative electrochemical studies across lyocell-, cotton-, and wool-based thread microfluidic platforms showed that lyocell exhibited a faster response onset and more stable steady-state currents, highlighting its superior performance in both fluid handling and electrochemical sensing. The lyocell-based thread microfluidic device can be integrated easily and securely with a microneedle electrochemical sensor, enabling efficient analyte delivery and reproducible responses for ferrocyanide and lactate. The thread-integrated lactate sensor exhibited a strong log-linear response across 0.01–10 mM with limits of detection of 0.433 mM under CA measurement and 0.51 mM under DPV measurement, demonstrating physiologically relevant ranges for sweat and saliva monitoring. Additional experiments further showed that the lyocell–modal platform retained concentration-dependent electrochemical performance after repeated use and maintained stable sensing performance at 3 °C and 26 °C, which provided acceptable selectivity in the presence of common interferents. The human saliva lactate detection further demonstrates the practical applicability of the platform for saliva-based POCT testing. Human saliva measurements showed that saliva lactate correlated positively with blood lactate (R = 0.94), supporting the feasibility of the proposed device for non-invasive saliva lactate analysis. In conclusion, this study demonstrates that the lyocell–modal lab-on-fabric microfluidic system provides a sustainable, low-cost, and scalable platform for electrochemical lactate sensing, particularly for non-invasive and POCT formats.

Author contributions

Ling Ding: conceptualization, methodology, investigation, formal analysis, visualization, writing – original draft. Huizi Zhang: formal analysis, resources. Li Yao: investigation, data curation, resources. Kameoka Jun: conceptualization, writing – review & editing, supervision, funding acquisition, project administration.

Conflicts of interest

There are no conflicts to declare.

Data availability

The data supporting the findings of this study are provided in the supplementary information (SI). Additional data are available from the corresponding author upon reasonable request.

Acknowledgements

This research was partially supported by JSPS Kakenhi: Grant number 90447285 and Amanokougyo grant 2023. All experiments were performed in accordance with the Guidelines of “the Declaration of Helsinki”, and experiments

were approved by the ethics committee at Waseda University. Informed consent was obtained from the human participants of this study.

References

1 P. Y. Keng, S. Chen, H. Ding, S. Sadeghi, G. J. Shah, A. Dooraghi, M. E. Phelps, N. Satyamurthy, A. F. Chatziioannou, C. Kim and R. M. van Dam, *Proc. Natl. Acad. Sci. U. S. A.*, 2012, **109**, 690–695, DOI: 10.1073/pnas.1117566109.
2 E. E. Hui and S. N. Bhatia, *J. Visualized Exp.*, 2007, **7**, 268.
3 K. Sato, A. Hibara and M. Tokeshi, *et al.*, Integration of Chemical and Biochemical Analysis Systems into a Glass Microchip, *Anal. Sci.*, 2003, **19**, 15–22, DOI: 10.2116/analsci.19.15.
4 M. Hanze, A. Piper and M. M. Hamedi, Stitched textile-based microfluidics for wearable devices, *Lab Chip*, 2024, **25**(1), 28–40, DOI: 10.1039/d4lc00697f.
5 M. Ramasamy, B. Ho, C.-M. Phan, N. Qin, C. L. Ren and L. Jones, *J. Micromech. Microeng.*, 2023, **33**, 105016.
6 N. Convery and N. Gadegaard, 30 years of microfluidics, *Micro Nano Eng.*, 2019, **2**, 76–91, DOI: 10.1016/j.mne.2019.01.003.
7 C. Iliescu, H. Taylor, M. Avram, J. Miao and S. Franssila, A practical guide for the fabrication of microfluidic devices using glass and silicon, *Biomicrofluidics*, 2012, **6**(1), 016505–016516, DOI: 10.1063/1.3689939.
8 C.-W. Tsao, Rev. of Polymer Microfluidics: Simple, Low-Cost Fabrication Process Bridging Academic Lab Research to Commercialized Production, *Micromachines*, 2016, **7**(12), 225, DOI: 10.3390/mi7120225.
9 J. Kim, R. Surapaneni and B. K. Gale, Rapid prototyping of microfluidic systems using a PDMS/polymer tape composite, *Lab Chip*, 2009, **9**(9), 1290, DOI: 10.1039/b818389a.
10 J. C. McDonald, D. C. Duffy, J. R. Anderson, D. T. Chiu, H. Wu, O. J. A. Schueller and G. M. Whitesides, *Electrophoresis*, 2000, **21**, 27–40.
11 L. Lin, *et al.*, PDMS Microfabrication and Design for Microfluidics, *Micromachines*, 2021, **12**, 643, — Describes PDMS microfluidic chips for rapid prototyping of biochips.
12 B. S. Hardy, K. Uechi, J. Zhen and H. P. Kavehpour, *Lab Chip*, 2009, **9**, 935–938.
13 V. Colella, L. Huggins, A. Hodžić, C. Galon, R. Traub, A. Alić, R. Iatta, L. Halos, D. Otranto, M. Vayssier-Taussat and S. Moutailler, *Transboundary Emerging Dis.*, 2022, **69**, e2943–e2951.
14 M. El-Tholoth, H. Bai, M. G. Mauk, L. Saif and H. H. Bau, *Lab Chip*, 2021, **21**, 1118–1130.
15 S. Kumar, M. Nehra, S. Khurana, N. Dilbaghi, V. Kumar, A. Kaushik and K. H. Kim, Aspects of Point-of-Care Diagnostics for Personalized Health Wellness, *Int. J. Nanomed.*, 2021, **16**, 383–402, DOI: 10.2147/IJN.S267212.
16 A. A. Smith, R. Li and Z. T. H. Tse, Reshaping healthcare with wearable biosensors, *Sci. Rep.*, 2023, **13**, 4998, DOI: 10.1038/s41598-022-26951-z.
17 A. Espinosa, J. Diaz, E. Vazquez, L. Acosta, A. Santiago and L. Cunci, *Talanta Open*, 2022, **6**, 100142.
18 E. B. Strong, S. A. Schultz, A. W. Martinez and N. W. Martinez, *Sci. Rep.*, 2019, **9**, 7.
19 X. Wu, S. Min, T. Zhan, Y. Huang, H. Niu and B. Xu, Humidity-enhanced microfluidic plasma separation on Chinese Xuan-papers, *Lab Chip*, 2024, **24**(18), 4379–4389, DOI: 10.1039/D4LC00393D.
20 A. Anushka, A. Bandopadhyay and P. K. Das, *Eur. Phys. J.: Spec. Top.*, 2023, **232**, 781–815.
21 W. Dungchai, O. Chailapakul and C. S. Henry, *Anal. Chem.*, 2009, **81**, 5821–5826.
22 D. M. Cate, J. A. Adkins, J. Mettakoonpitak and C. S. Henry, *Anal. Chem.*, 2015, **87**, 19–41.
23 A. K. Yetisen, M. S. Akram and C. R. Lowe, *Lab Chip*, 2013, **13**, 2210–2251.
24 T. Akyazi, L. Basabe-Desmonts and F. Benito-Lopez, *Anal. Chim. Acta*, 2018, **1001**, 1–17.
25 S. Nishat, A. T. Jafry, A. W. Martinez and F. R. Awan, *Sens. Actuators, B*, 2021, **336**, 129681.
26 H. Lim, A. T. Jafry and J. Lee, *Molecules*, 2019, **24**, 2869.
27 M. Mostafalu, H. Tamayol, F. Rahimi, M. Ochoa, Z. Khalilzadeh and K. D. Konstantopoulos, *et al.*, *Microsyst. Nanoeng.*, 2016, **2**, 16074.
28 Z. Zhao, Q. Li, L. Chen, Y. Zhao, J. Gong, Z. Li and J. Zhang, *Lab Chip*, 2021, **21**, 916.
29 T. Zhan, H. Niu, Y. Huang, S. Min, X. Wu, H. Wang and B. Xu, 3D microfluidic analytical device on a single thread for smart point-of-care blood typing, *Lab Chip*, 2025, **25**(11), 2769–2779, DOI: 10.1039/D5LC00192G.
30 S. Min, T. Zhan, Y. Lu, D. Pan, X. Chen and B. Xu, Rapid and easily identifiable blood typing on microfluidic cotton thread-based analytical devices, *Lab Chip*, 2023, **23**(21), 4680–4689, DOI: 10.1039/D3LC00501A.
31 A. Sankauskaite, R. Pauliukaite, J. Baltusnikaite-Guzaitiene and A. Abraitiene, *Curr. Opin. Electrochem.*, 2023, **39**, 100981.
32 M. Galliani, E. Ismailova, P. Azizian, A. Makhinia and J. M. Cabot, *npj Flexible Electron.*, 2025, **9**, 38.
33 M. F. Ulum, L. Maylina, D. Noviana and D. H. B. Wicaksono, *Lab Chip*, 2016, **16**, 1492–1504.
34 J. U. Khan, S. Sayyar, D. Jin, B. Paull and P. C. Innis, *Microfluid. Nanofluid.*, 2022, **26**, 96.
35 I. Öberg Månsson, A. Piper and M. M. Hamedi, *Macromol. Biosci.*, 2020, **20**, 2000150.
36 Y. Weng, Y. Pan, J. Zhang, Y. Guo and X. Fang, *Micromachines*, 2020, **11**, 404, DOI: 10.3390/mi11040404.
37 D. R. Ballerini, X. Li and W. Shen, *Biomicrofluidics*, 2011, **5**, 014105.
38 J. Berthier, K. A. Brakke, D. Gosselin, E. Berthier and F. Navarro, *Med. Eng. Phys.*, 2017, **48**, 55–61.
39 A. Milic, H. AlJalal, S. Alamoudi, R. Alnajrani and M. El-Moselhy, *Sensors*, 2024, **24**, 4352, DOI: 10.3390/s24134352.
40 M. Ghahremani Honarvar and M. Latifi, Overview of Wearable Electronics and Smart Textiles, *J. Text. Inst.*, 2017, **108**, 631–652, DOI: 10.1080/00405000.2016.1177870.

41 K. Xia, Y. Yan, X. Wang and X. Liu, *MRS Bull.*, 2021, **46**, 1070–1079, DOI: 10.1557/s43577-021-00116-1.
42 S. Hasanpour, M. Mahmoodi, A. Golovin and D. A. Powell, *ACS Omega*, 2021, **6**, 1645–1654, DOI: 10.1021/acsomega.0c06309.
43 G. Acar, O. Ozturk, A. J. Golparvar, T. A. Elboshra, K. Böhringer and M. K. Yapici, Wearable and flexible textile electrodes for biopotential signal monitoring: a review, *Electronics*, 2019, **8**, 479.
44 S. Akter, S. L. M. Baharin, N. M. Ali and M. L. Azmi, *Micromachines*, 2024, **15**, 684, DOI: 10.3390/mi15040684.
45 V. Žuravliova and J. Baltušnikaitė-Guzaitienė, *J. Funct. Biomater.*, 2024, **15**, 348.
46 A. Sharma, T. Hocker, F. E. Kleine and P. A. Lovell, *Cellulose*, 2019, **26**, 755–773.
47 S. Zhang, C. Chen, C. Duan, H. Hu, H. Li, J. Li, Y. Liu, X. Ma, J. Stavik and Y. Ni, *BioResources*, 2018, **13**, 4577–4592.
48 D. W. Chae, H. G. Chae, B. C. Kim, Y. S. Oh, S. M. Jo and W. S. Lee, *Text. Res. J.*, 2002, **72**, 335–340.
49 E. Borbély, Lyocell, The New Generation of Regenerated Cellulose, *Acta Polytech. Hung.*, 2008, **5**, 11–18.
50 X. Jiang, Y. Bai and X. Chen, *J. Biobased Mater. Bioenergy*, 2020, **5**, 16.
51 P. Salvo, F. Di Francesco, D. Costanzo, C. Ferrari, M. G. Trivella and D. De Rossi, *IEEE Sens. J.*, 2010, **10**, 1557–1563.
52 R. Garjonytė, Y. Yigzaw, R. Meškys, A. Malinauskas and L. Gorton, Prussian Blue- and lactate oxidase-based amperometric biosensor for lactic acid, *Sens. Actuators, B*, 2001, **79**, 33–38.
53 L. J. Currano, F. C. Sage, M. Hagedon, L. Hamilton, J. Patrone and K. Gerasopoulos, *Sci. Rep.*, 2018, **8**, 15890.
54 K. Petropoulos, S. Piermarini, S. Bernardini, G. Palleschi and D. Moscone, *Sens. Actuators, B*, 2016, **237**, 8–15.
55 ARKRAY, Lactate Pro 2 LT-1730, product information.
56 E. Maiorano, M. M. Calabretta, E. Lunedei and E. Michelini, *Biosensors*, 2025, **15**, 530.
57 J. Ballesta-Claver, M. C. Valencia-Mirón and L. F. Capitán-Vallvey, *Analyst*, 2009, **134**, 1423–1432.
58 X. Xuan, C. Chen, H. Chen, Y. Jin, B. Jin, S. Xu, J. Zhang and G. Crespo, *ACS Sens.*, 2023, **8**, 2401–2409.
59 G. Iula, F. Miglione, A. D. Nisio, F. Francia, E. Tamburri, G. Palleschi, D. Moscone and S. Cinti, *Anal. Bioanal. Chem.*, 2025, **417**, 3825–3834.
60 N. V. Zaryanov, V. N. Nikitina, E. E. Karpova, E. V. Shcherbacheva, V. A. Andreev and E. E. Karyakina, *Anal. Chem.*, 2017, **89**, 11198–11202.